Obrabotka metallov (tekhnologiya, oborudovanie, instrumenty) = Metal Working and Material Science. 2025 vol. 27 no. 3 pp. 205–220
ISSN: 1994-6309 (print) / 2541-819X (online)
DOI: 10.17212/1994-6309-2025-27.3-205-220

NSTU NETI

Obrabotka metallov - Metal Working and Material Science

Journal homepage: http://journals.nstu.ru/obrabotka_metallov

Features of the structure of gradient layers «steel - Inconel - steel», obtained by laser direct metal deposition

Svetlana Dolgova [1, a], ***Alexandr Malikov*** [2, b], ***Alexander Golyshev*** [2, c], ***Aelita Nikulina*** [3, d,*]

[1] Novosibirsk semiconductor device plant Vostok, 60 Dachnaya st., Novosibirsk, 630082, Russian Federation
[2] Khristianovich Institute of Theoretical and Applied Mechanics SB RAS, 4/1 Institutskaya str., Novosibirsk, 630090, Russian Federation
[3] Novosibirsk State Technical University, 20 Prospekt K. Marksa, Novosibirsk, 630073, Russian Federation

[a] https://orcid.org/0000-0003-3918-273X, svetlanadolgova99@gmail.com; [b] https://orcid.org/0000-0003-1268-8546, smalik707@yandex.ru;
[c] https://orcid.org/0000-0002-4243-0602, alexgol@itam.nsc.ru; [d] https://orcid.org/0000-0001-9249-2273, a.nikulina@corp.nstu.ru

ARTICLE INFO

Article history:
Received: 13 June 2025
Revised: 27 June 2025
Accepted: 22 July 2025
Available online: 15 September 2025

Keywords:
Additive manufacturing
Microstructure
Gradient layers
Phase composition
Austenitic stainless steel *316L*
Nickel alloy *Inconel 625*

Funding
The work was carried out within the framework of the state assignment of the S.A. Khristianovich Institute of Theoretical and Applied Mechanics SB RAS No. 124021500015-1.

Acknowledgements
Experiments on direct laser deposition were carried out at the Center of Collective Use "Mechanics" of ITAM SB RAS. Structural research was conducted at core facility "Structure, mechanical and physical properties of materials" NSTU and scientific and educational center in the field of mechanical engineering of NSTU.

ABSTRACT

Introduction. Traditionally, the most common technology for producing parts from nickel alloys involves casting followed by heat treatment to achieve the required phase composition. Significant disadvantages of this method include the segregation of chemical elements, the presence of large undesirable inclusions such as *Laves* phase and eutectic structures, and the non-uniform distribution of strengthening phases throughout the workpiece cross-section. At the same time, many complex-shaped parts are assembled into a single combined structure using welding. An analysis of the hardening characteristics of nickel alloys and the products derived from them suggests that additive manufacturing techniques are a promising approach for fabricating such workpieces. The structure and phase composition of the material volumes formed via layer-by-layer deposition will differ significantly from those obtained by conventional methods. In the case of producing combined structures using additive methods, identifying the patterns of structure and phase composition formation becomes an even more complex challenge. Therefore, **the purpose of this work** is to identify the structural features of "steel - nickel alloy – steel" gradient layers fabricated by direct metal deposition. The study examines dissimilar joints produced using the "Welding and Surfacing Complex based on a Multi-Coordinate Arm and a Fiber Laser" at the S.A. Khristianovich Institute of Theoretical and Applied Mechanics of the Siberian Branch of the Russian Academy of Sciences, employing direct metal deposition technology. **Research methods.** A Carl Zeiss *Axio Imager A1m* light microscope and a Carl Zeiss *EVO 50 XVP* scanning electron microscope, equipped with an *INCA X-Act* energy-dispersive X-ray spectroscopy (*EDS*) attachment, were utilized for microstructural investigations of the fabricated layers. Phase composition analysis of the samples was performed using an *ARL X'TRA* X-ray diffractometer. Microhardness testing was conducted using a *Wolpert Group 402 MVD Vickers* hardness tester. **Results and discussion.** It was observed that the maximum layer height (up to 7 mm) was achieved when implementing the following parameters: 1,000 W laser power with a scanning speed of 35 mm/s, and 1,500 W laser power with a scanning speed of 15 mm/s. In the first case, minimal material mixing at the fusion boundary was noted. In all fabricated compositions, defects in the form of unmelted powder particles were observed, as well as cracks in the first steel layers. During the deposition of *Inconel 625* onto *316L* stainless steel, the transition zone exhibited solidification modes consistent with the formation of iron-based alloys, specifically *FA* (ferrite-austenite), *AF* (austenite-ferrite), and *A* (austenite) sequentially. When depositing *316L* stainless steel onto *Inconel 625*, the transition zone exhibited a solidification mode characterized by the formation of only the austenite phase. The microhardness values were found to be 230 ±15 HV for *316L* stainless steel and 298 ± 20 HV for *Inconel 625*.

For citation: Dolgova S.V., Malikov A.G., Golyshev A.A., Nikulina A.A. Features of the structure of gradient layers «steel - Inconel - steel», obtained by laser direct metal deposition. *Obrabotka metallov (tekhnologiya, oborudovanie, instrumenty) = Metal Working and Material Science*, 2025, vol. 27, no. 3, pp. 205–220. DOI: 10.17212/1994-6309-2025-27.3-205-220. (In Russian).

*** Corresponding author**
Nikulina Aelita A., D.Sc. (Engineering), Professor
Novosibirsk State Technical University,
20 Prospekt K. Marksa,
630073, Novosibirsk, Russian Federation
Tel.: +7 383 346-11-71, **e-mail:** a.nikulina@corp.nstu.ru

Introduction

Nickel-based alloys are widely used for manufacturing critical components across various industries, including aerospace, power generation, petrochemical, and marine sectors. This widespread application is attributed to their combination of high corrosion resistance and mechanical strength at moderately elevated temperatures. The high strength of these alloys is achieved through a specific phase composition, which in turn is determined by the presence of particular alloying elements and the corresponding strengthening mechanisms [1–3].

Traditionally, the most common method for producing components from nickel alloys is casting, followed by heat treatment to form the desired phase structure [4]. However, this approach has several significant drawbacks. These include chemical element segregation, the presence of large undesirable *Laves* phase inclusions and eutectics [5, 6], as well as an uneven distribution of strengthening phases across the cross-section of the workpiece [7]. Moreover, many complex-shaped components are assembled into a single combined structure using welding techniques.

Additive manufacturing technologies present a promising alternative for producing nickel alloy components, as evidenced by analysis of strengthening mechanisms in these alloys and their manufactured parts [8–12]. This approach offers several key advantages: (1) it addresses the challenge of fabricating geometrically complex components; (2) the rapid cooling rates characteristic of additive processes minimize chemical segregation; (3) the layer-by-layer deposition induces repeated thermal cycling, which can promote *in situ* precipitation of strengthening phases during the build. Moreover, the ability to create hybrid structures reduces the consumption of expensive materials. As a result, the microstructure and phase composition of additively manufactured materials are anticipated to differ significantly from those produced via conventional methods.

Despite the growing interest in this topic in the scientific literature, a comprehensive understanding of the microstructural and phase characteristics of various alloys produced by additive technologies is still lacking. This is primarily due to the wide variability in processing methods and parameters used in different studies. Furthermore, in the case of hybrid structures produced via additive manufacturing, identifying the patterns of structure and phase formation becomes an even more complex task [13–15].

Consequently, the purpose of this work is to investigate the structural features of gradient layers in «steel – nickel alloy – steel» systems fabricated by direct laser deposition.

Research methods

Research materials

For sample fabrication, powders of *Inconel 625* nickel-based alloy (particle size: 50–70 μm) and *AISI 316L* stainless steel (particle size: 15–45 μm) were used (Fig. 1). A 50×50×5 mm plate made of *0.12 C-18 Cr-10 Ni-Ti* stainless steel served as the substrate. The chemical compositions of the initial materials are presented in Table 1.

Sample preparation

Dissimilar joints were fabricated at the Khristianovich Institute of Theoretical and Applied Mechanics SB RAS using a “Cladding and Welding Complex Based on a Multi-Axis Robotic Arm and a 3 kW Fiber Laser (IPG Photonics) with a Wavelength of 1.07 μm”. Direct laser deposition (*DLD*) was employed as the processing method, where powder is delivered through a coaxial nozzle into a localized melt pool generated by laser radiation. The high scanning speed and rapid cooling rates inherent in this technique minimize thermal gradients and reduce the likelihood of secondary phase formation in the joint region. Argon served as the shielding gas. Detailed deposition parameters are provided in Table 2 [16].

The samples were fabricated in a unidirectional manner. Sequentially, four layers of each material were deposited in the order: steel – nickel alloy – steel. Each subsequent layer overlapped the previous layer by 50%, which was intended to ensure a smooth transition between the materials.

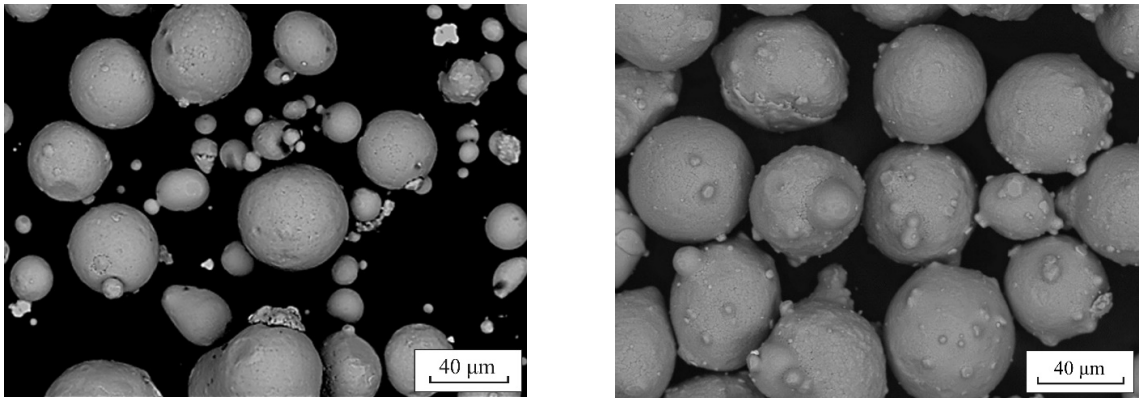

a *b*

Fig. 1. Particles of *Inconel 625* (*a*) and *AISI 316L* (*b*) powders

Table 1

Chemical composition of the materials

Material	Chemical element, wt.%								
	Fe	*Ni*	*Cr*	*C*	*Mo*	*Nb*	Ti	S	P
316L	*bal.*	8.84	18.69	0.03	2.50	-	0.71	0.013	0.015
Inconel 625	3.8	*bal.*	19.16	0.1	8.1	3.36	0.28	0.011	0.01
0.12 C-18 Cr-10 Ni-Ti	*bal.*	7.852	18.16	0.027	–	–	0.002	0.002	0.027

Table 2

Deposition parameters for specimens

Mode	Power, W	Speed, mm/s	Consumption, g/min	Beam diameter, mm
1	1,000	35	12	4,1
2	1,250	25		
3	1,500	15		

Structural studies

Structural characterization was performed using an optical microscope *Carl Zeiss A1Z* and a scanning electron microscope (*SEM*) *Carl Zeiss EVO 50 XVP*. Sample preparation followed standard metallographic procedures, including grinding and polishing steps. To reveal the microstructure of the joints, electrolytic etching was carried out in a 10 % aqueous solution of oxalic acid.

The chemical composition in the joint zones between dissimilar materials was analyzed using energy-dispersive X-ray spectroscopy (*EDS*) with an *INCA X-Act* detector attached to the *SEM*.

Phase composition analysis was conducted on an *ARL X'TRA* X-ray diffractometer equipped with a *Mo* $K\alpha 1/\alpha 2$ radiation source ($\lambda = 0.7093$ Å), using a step size of $\Delta 2\theta = 0.03°$ and an acquisition time of 5 s per point.

Microhardness testing was carried out using a *Wolpert Group 402 MVD* Vickers hardness tester under a load of 100 g with a dwell time of 10 s applied to a diamond indenter.

Results and Discussion

An example of the fabricated hybrid structure is shown in Fig. 2. During deposition, a uniform wall was formed without visible surface cracks. The height of the built structures reached 7 mm for processing

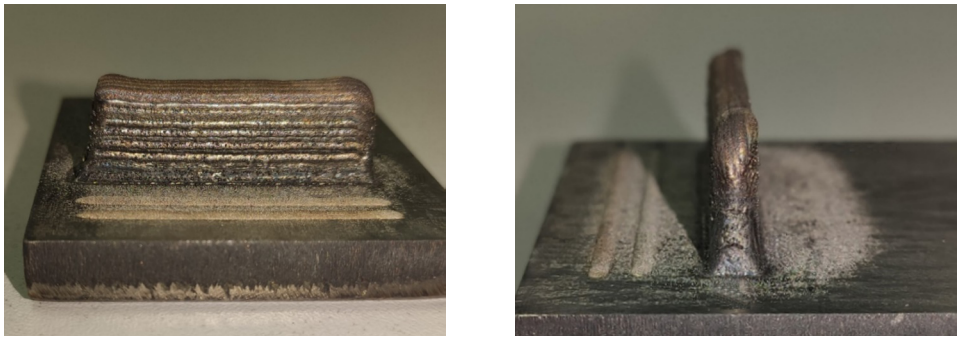

Fig. 2. Example of a fabricated specimen

modes 1 and 3, and 5 mm for mode 2. For microstructural analysis, the bimetallic specimen was sectioned along a plane perpendicular to the direction of layer growth.

The homogeneous layers produced from chromium-nickel steel or nickel-based alloy powder exhibit a characteristic dendritic microstructure with the formation of both equiaxed and columnar dendrites. At the interfaces between successive layers and near the boundaries of the deposited structure, where heat dissipation was more intense, columnar dendrites predominate. These dendrites are typically characterized by the presence of secondary arms (Fig. 3). At the edges of the deposited structures, regardless of the processing mode, spherical particles with diameters ranging from 25 to 40 μm were observed (Figs. 4, *a*, *b*). These are unmelted or partially melted particles of the original powder, which is a characteristic feature of the direct laser deposition (*DLD*) process [17, 18]. In addition, the formation of cracks was noted both at the interface between dissimilar materials (Fig. 4, *c*, *d*) and at the fusion boundaries between similar materials. This phenomenon is attributed to thermal stresses that arise during the formation of dissimilar gradient materials.

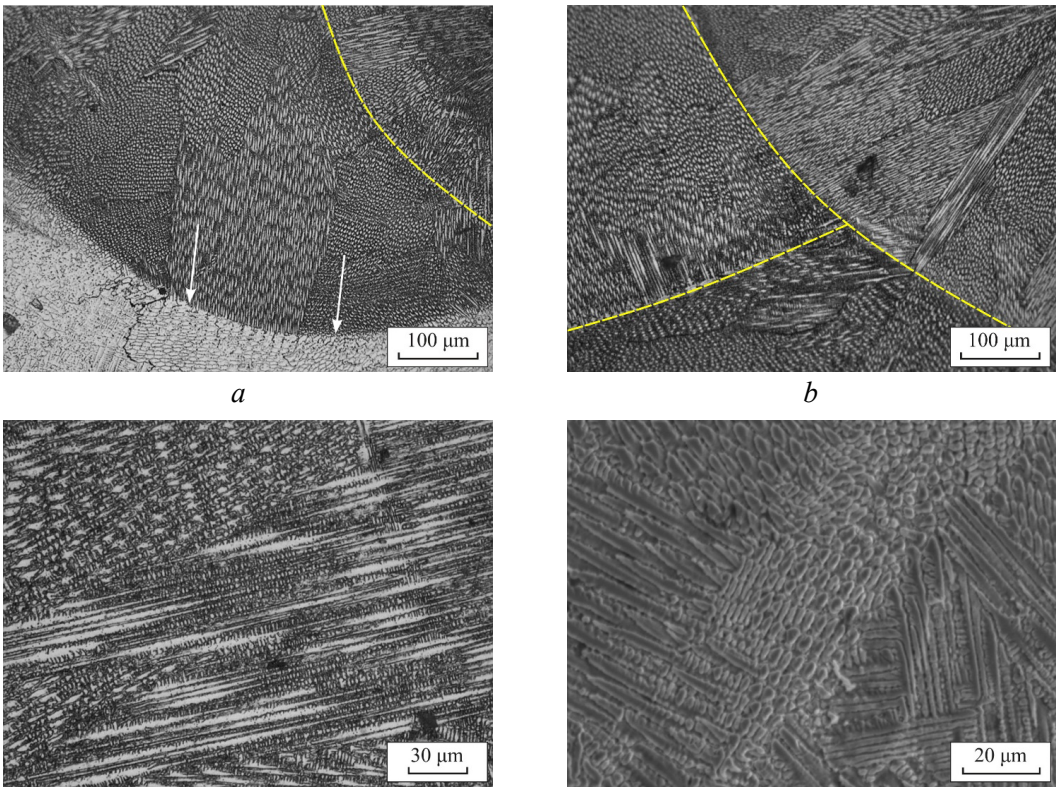

a *b*

c *d*

Fig. 3. Location of elongated dendrites:

a – transition layers boundary; *b* – dissimilar material interface; *c* – layer edge; *d* – secondary arms in elongated dendrites

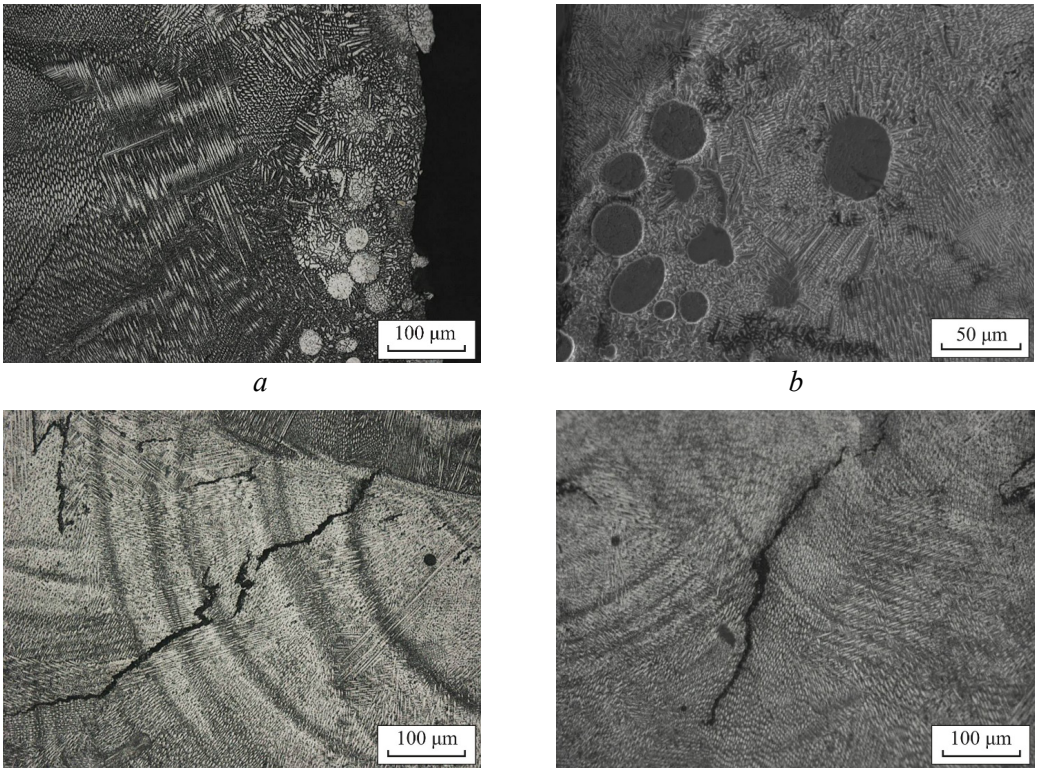

Fig. 4. Defects in fabricated materials: unmelted particles at layer boundaries in mode **1** (*a*) and mode **2** (*b*); thermal cracks at the dissimilar material interface (*c*) and within the homogeneous material (*d*)

The sequential deposition of four layers during material transitions resulted in the formation of smooth gradients between dissimilar materials. At the same time, a visible interface and mixing zones were observed for both material combinations (Figs. 5–7). The appearance of these zones may be attributed to the high melting rate, which can lead to the formation of an unstable melt pool [17, 19, 20]. Such zones were observed under all deposition modes; however, it was noted that with decreasing laser power, both the number and width of these regions were reduced.

In the case of *Inconel 625* deposited onto *316L* steel, the mixing zones exhibited sharper boundaries (Fig. 8, *a*) compared to those formed during deposition of austenitic steel onto the nickel-based alloy (Fig. 8, *b*).

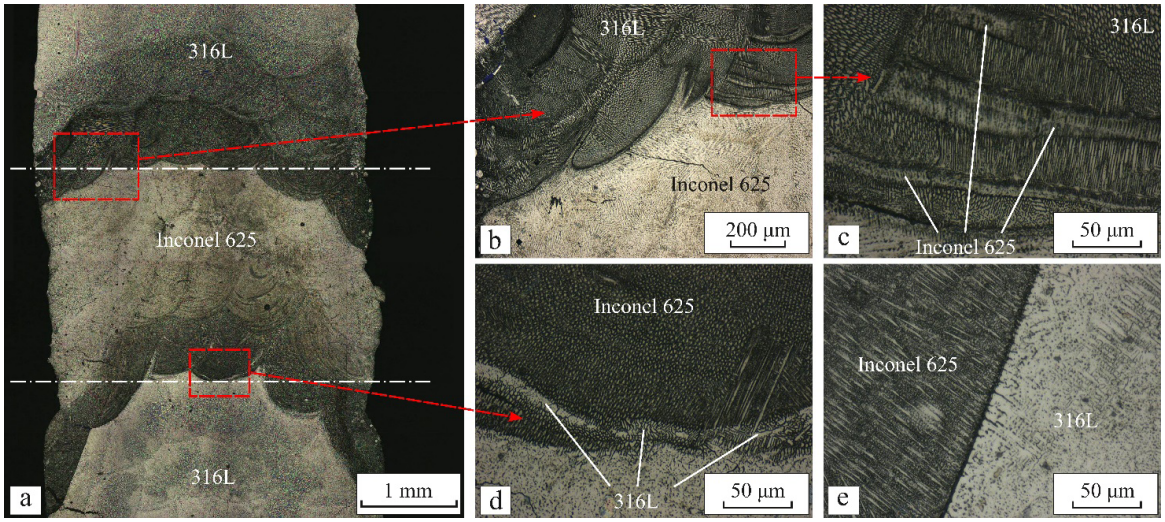

Fig. 5.Cross-section of specimenfabricated using mode **1**:

a – general view; *b* – *Inconel 625* – *316L* stainless steel interface; *c* – mixing zones of nickel alloy and steel; *d* – *316L* stainless steel – *Inconel 625* interface with mixing zone; *e* – clear interface region

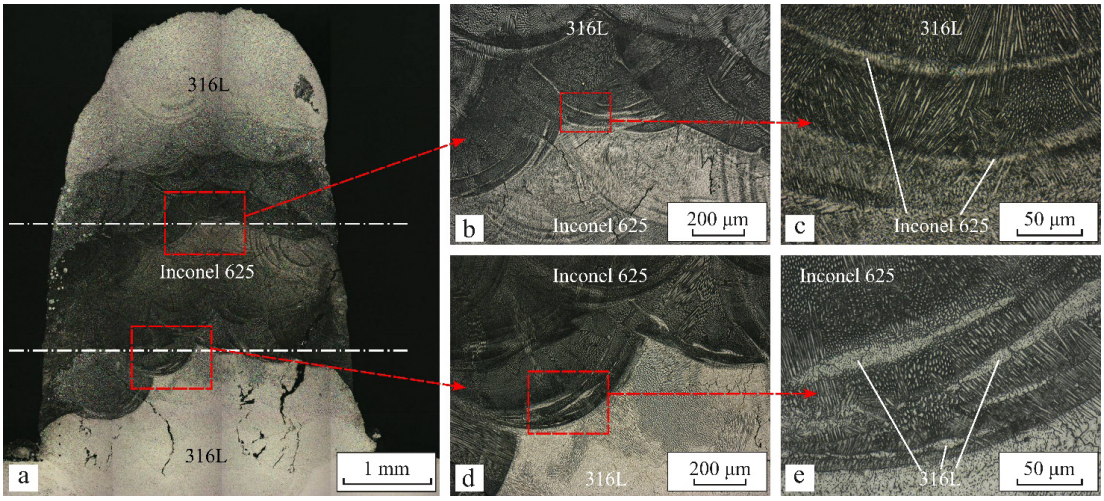

Fig. 6. Cross-section of specimen fabricated using mode **2**:

a – general view; *b* – *Inconel 625* – *316L* stainless steel interface; *c* – mixing zones of nickel alloy and steel; *d* – *316L* stainless steel – *Inconel 625* interface; *e* – mixing zones of steel and nickel alloy

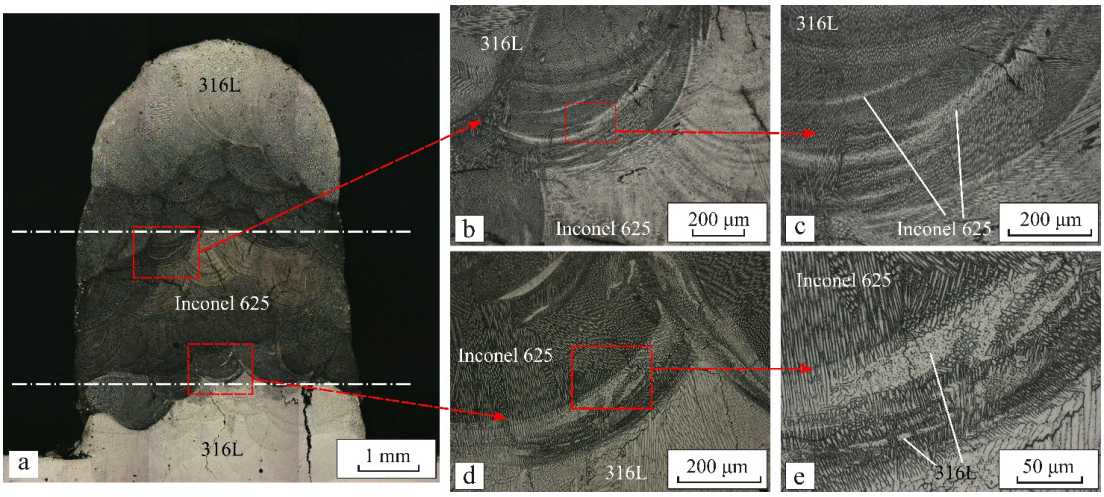

Fig. 7. Cross-section of specimen fabricated using mode **3**:

a – general view; *b* – *Inconel 625* – *316L* stainless steel interface; *c* – mixing zones of nickel alloy and steel; *d* – *316L* stainless steel – *Inconel 625* interface; *e* – mixing zones of steel and nickel alloy

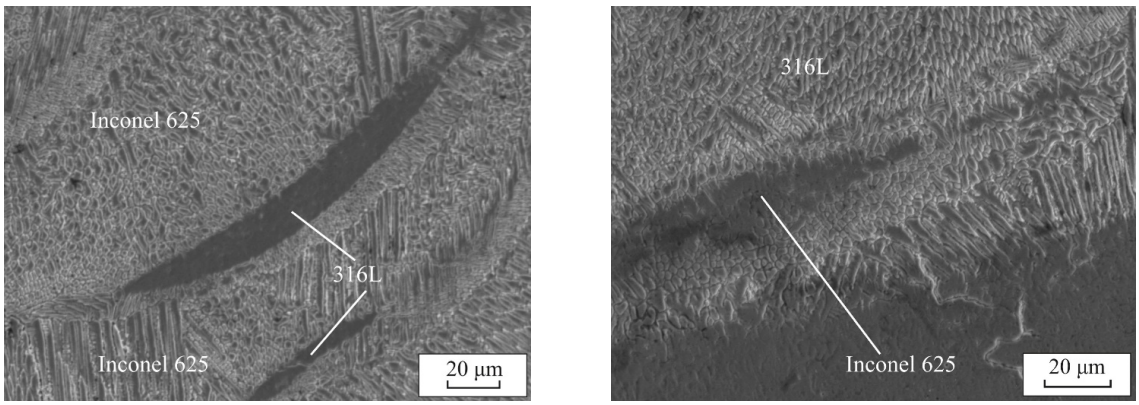

a *b*

Fig. 8. Microstructure of mixed regions:

a – *Inconel 625* deposited on steel; *b* – *316L* stainless steel deposited on *Inconel 625*

Fig. 9 shows the distribution of chemical elements along a line positioned perpendicular to the transition zone in the case of nickel alloy deposition onto steel. In all cases, a wide transition zone is observed. As can be seen, under processing mode **1** (1,000 W, 35 mm/s), the concentrations of iron and nickel equilibrate within 50 μm from the visible fusion boundary between the dissimilar materials, already within the first deposited layer (Fig. 9, *a*). Under mode **2** (1,250 W, 25 mm/s), the concentrations of nickel and iron begin to equalize at a distance of 500–600 μm from the visible fusion line (Fig. 9, *b*). This region corresponds approximately to the boundary of the second deposited layer of the nickel alloy. In contrast, under mode **3** (1,500 W, 15 mm/s), the concentration equalization occurs significantly beyond the second nickel alloy layer and corresponds to a distance of 800–900 μm from the visible fusion boundary between the dissimilar materials (Fig. 9, *c*). In these transition regions, the nickel concentration is lower than that of the original nickel alloy and ranges between 35–45 wt. %. Below the visible fusion boundary, the steel regions retain their original composition, with a slightly elevated nickel content of up to 11 wt. %.

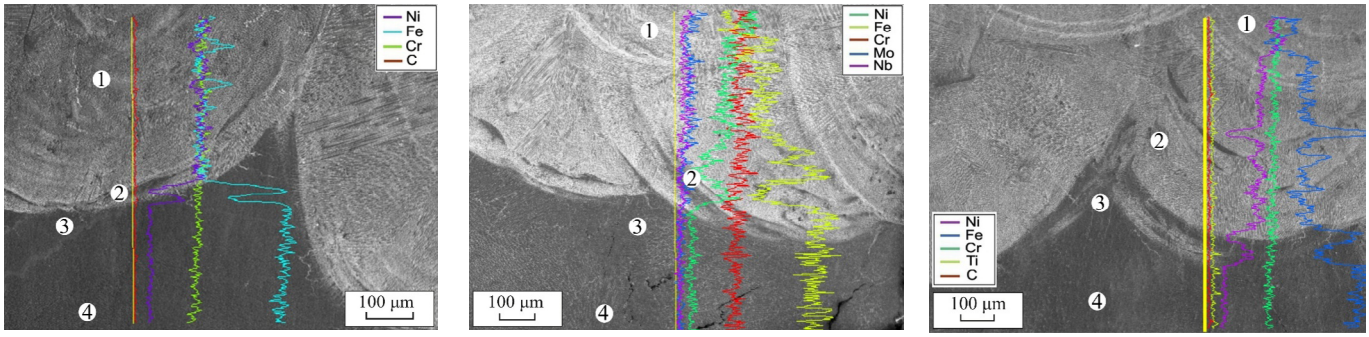

a *b* *c*

Fig. 9. Energy-dispersive X-ray spectroscopy (*EDS*) analysis results for the *316L* stainless steel – *Inconel 625* joint:
a – mode **1**; *b* – mode **2**; *c* – mode **3**

According to quantitative energy-dispersive X-ray spectroscopy (*EDS*) analysis, the zones of mechanical mixing of steel into the nickel alloy are characterized by reduced iron content and increased nickel content (Table 3). An increase in both distance from the fusion boundary and laser power promotes higher nickel content in these regions.

During the deposition of steel onto the nickel-based alloy, a wide transition zone and numerous regions of mechanical mixing were also observed (Fig. 10). The visible fusion boundary between the nickel alloy and steel is well-defined under the first two processing modes. Under mode **1** (1,000 W, 35 mm/s), the concentrations of iron and nickel begin to equilibrate within the first deposited layer of the nickel alloy at a distance of 300–400 μm from the visible fusion line, with the iron concentration starting to gradually increase within 50–100 μm beyond that point. Under mode **2** (1,250 W, 25 mm/s), the equalization of iron and nickel concentrations occurs at a distance of 600–700 μm from the visible fusion boundary between the dissimilar materials, corresponding to the level of the second deposited steel layer. Under mode **3** (1,500 W, 15 mm/s), the visible interface between the nickel alloy and steel becomes more diffuse, and the iron concentration exceeds that of nickel at the boundary of the second deposited steel layer, similarly to mode **2**. In this region, the iron concentration within the second deposited steel layer is in the range of 40–45 wt. %.

In the regions of the nickel alloy located below the visible fusion boundary, the chemical composition under mode **1** corresponds to that of the original alloy. However, for modes **2** and **3**, an elevated iron content and a slightly reduced nickel content were observed – 9 wt. % and 52 wt. %, respectively. The composition of the mechanical mixing zones, where nickel alloy is incorporated into the steel matrix, is characterized by an increased iron content and a correspondingly reduced nickel content compared to the original *Inconel 625* alloy (Table 4).

The varying ratio of chromium and nickel equivalents indicates the formation of zones with different phase compositions. According to established models of phase formation during welding of dissimilar

Table 3

Chemical composition of mixing zones in the transition region when depositing *Inconel 625* on *316L* stainless steel

Point	Chemical element, wt.%							
	Fe	*Ni*	*Cr*	*Ti*	*Mo*	*Nb*	*Si*	*Mn*
Mode **1**								
1	35.04	35.15	20.12	0.4	5.27	2.22	0.87	0.94
2	62.4	15.55	19.45	0.77	–	–	1.13	0.7
3	67.69	10.73	18.86	0.9	0.27	–	1.11	0.44
4	67.35	11.16	18.82	1.03	–	–	1.03	0.61
Mode **2**								
1	22.32	45.51	21.1	0.24	6.45	2.9	0.75	0.74
2	58.92	17.91	19.23	0.55	1.36	0.5	0.86	0.66
3	68.4	9.9	18.88	0.58	0.29	0.25	0.92	0.79
4	68.13	10.41	18.79	0.42	0.4	–	1.05	0.8
Mode **3**								
1	22.32	44.94	20.91	0.27	7.36	3.11	0.73	0.31
2	49.3	25.42	18.98	0.58	3.22	1.31	0.67	0.52
3	67.26	11.66	18.28	0.73	0.53	–	0.92	0.61
4	68.51	10.24	18.33	0.58	0.55	0.31	0.97	0.55

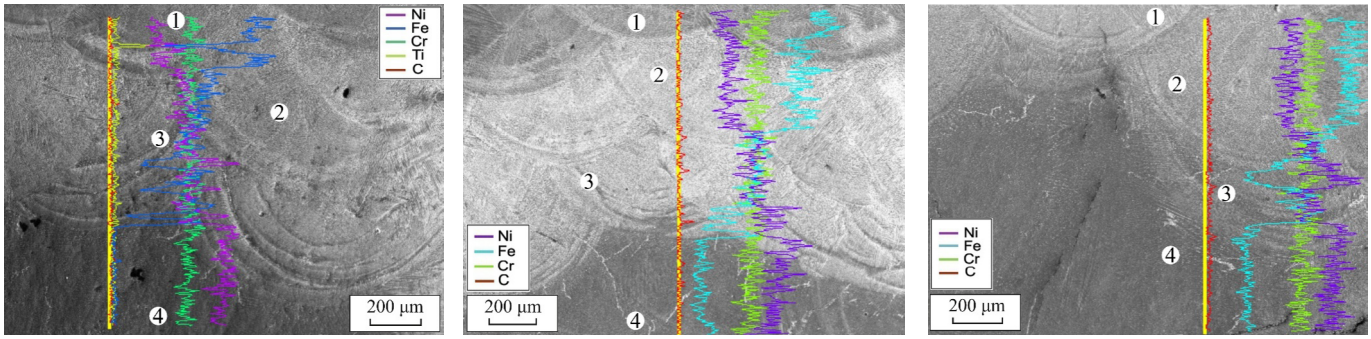

a *b* *c*

Fig. 10. Energy-dispersive X-ray spectroscopy (*EDS*) analysis results for the *Inconel 625 – 316L* stainless steel joint:

a– mode **1**; *b* – mode **2**; *c* – mode **3**

steels [21, 22], in the case of *Inconel 625* being deposited onto *316L* steel, the transition zone, where iron-based alloys form based on chemical composition, undergoes sequential solidification modes: *FA* (δ-*Fe* + γ-*Fe*), *AF* (γ-*Fe* + δ-*Fe*), and *A* (γ-*Fe*) (Fig. 11, regions **1**–**3**). Although nickel atoms have higher mobility in iron, the melting point of *316L* steel is slightly higher than that of the nickel alloy, resulting in a relatively narrow transition zone. At the same time, nickel diffusion is sufficiently intense, leading to changes in the chromium-to-nickel equivalent ratios in these areas. The formation of ferrite in the transition layers of the «steel – nickel alloy» system was confirmed by X-ray diffraction analysis (Fig. 12) and scanning electron microscopy (Fig. 13).

In regions **4**–**7** (Fig. 11), nickel-based alloys are formed. Regions **5** and **6** correspond to the original *Inconel 625* composition, while regions **4** and **7** are characterized by a reduced nickel content compared to the base alloy.

During deposition of steel onto the nickel alloy, the higher processing temperature leads to the formation of a wider transition zone. However, the nickel content in this zone remains relatively high, which ultimately

Table 4

Chemical composition of mixing zones in the transition region when depositing *316L* stainless steel on *Inconel 625*

Point	Chemical element, wt.%								
	Fe	*Ni*	*Cr*	*Ti*	*Mo*	*Nb*	*Si*	*Mn*	*S*
Mode **1**									
1	51.74	23.78	20.09	0.54	1.44	0.79	0.78	0.54	0.31
2	47.39	26.05	19.71	0.51	3.36	1.43	0.85	0.7	–
3	19.11	46.48	21.12	0.17	7.88	3.64	1.02	0.6	–
4	0.7	61.09	22.37	–	10.26	4.44	0.74	0.34	–
Mode **2**									
1	55.01	20.76	19.36	0.61	2.07	1.06	0.8	0.32	–
2	45.64	27.86	20.07	0.47	3.2	1.35	0.93	0.48	–
3	22.81	44.47	21.05	0.29	6.66	3.5	0.76	0.47	–
4	7.79	55.57	22.15	–	9.54	3.82	0.83	0.3	–
Mode **3**									
1	43.8	29.34	20.31	0.5	2.81	1.35	0.82	0.51	–
2	38.89	31.86	20.1	0.42	4.76	2.35	0.96	0.67	–
3	14.44	50.49	21.76	0.17	7.34	3.65	0.95	0.66	0.53
4	8.57	55.79	21.17	0.11	9.14	3.83	0.84	0.56	–

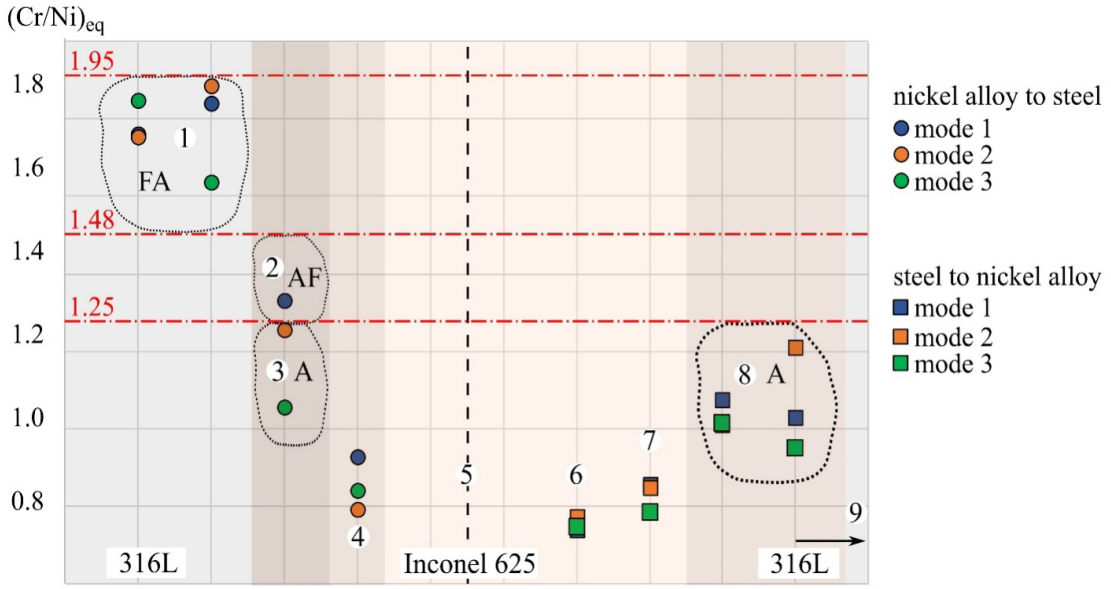

Fig. 11. Chromium and nickel equivalent ratios in different regions of the combined material. Solidification modes: *AF*, *FA* (austenite-ferrite); *A* (austenite)

results in the *A*-mode solidification regime (Fig. 11, region **8**). Region **9** corresponds to the chemical composition of the original *316L* stainless steel.

A sharp change in microhardness levels is observed across the gradient transition from steel to the nickel alloy (Fig. 14), which is typical for dissimilar material systems. At the same time, the differences in microhardness values between materials produced under different processing modes are relatively minor. It is worth noting that near the fusion boundary, the microhardness of *316L* steel deposited onto the nickel alloy is slightly higher than that of the steel layers onto which the nickel alloy was deposited. The average

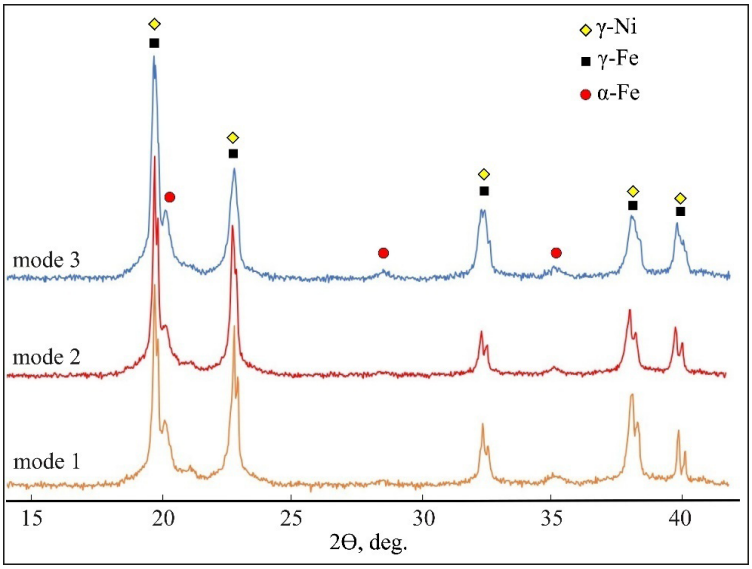

Fig. 12. X-Ray diffraction (*XRD*) patterns of heterogeneous compositions fabricatedusing different deposition modes

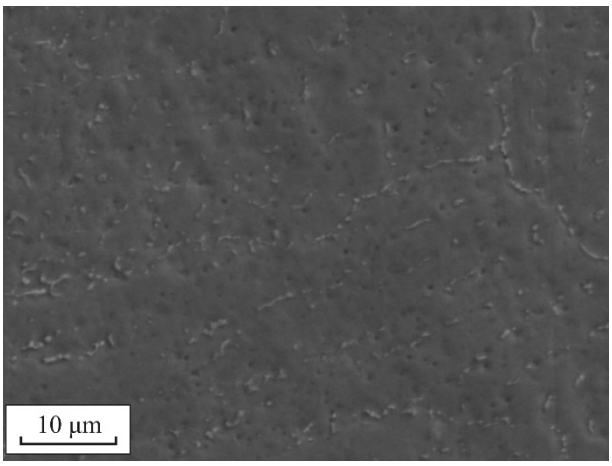

Fig. 13. Ferrite formed in the transition region during deposition of nickel alloy on steel

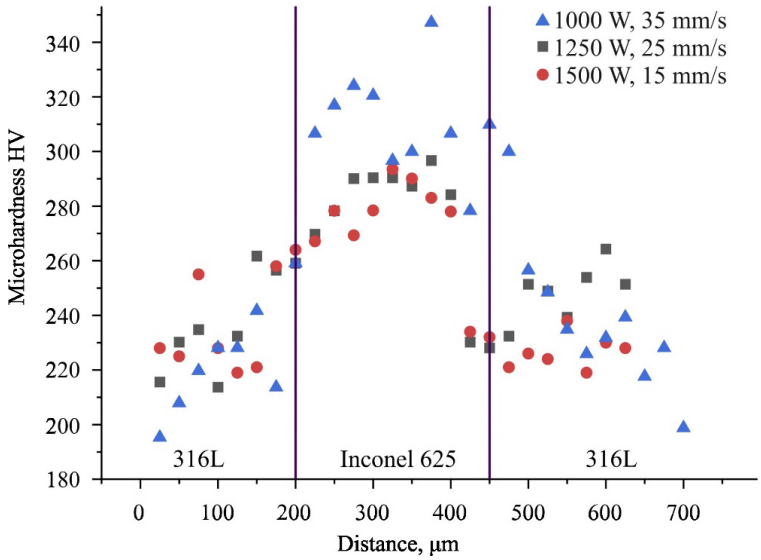

Fig. 14. Results of microhardness testing of the combined materials

microhardness for the steel regions in both cases is approximately 230 ± 15 HV, while for *Inconel 625* it is around 298 ± 20 HV.

Under the second and third processing modes, a slight decrease in the microhardness of the nickel alloy was observed, which can be attributed to higher heat input compared to mode **1**. These results are in good agreement with previously published data, regardless of the specific deposition method used [10, 11, 19].

Conclusoin

This study analyzed the structural features of gradient «*316L* steel – *Inconel 625* – *316L* steel» compositions fabricated *via* direct laser deposition. Results revealed that, during layer-by-layer fabrication of gradient structures comprising 12 layers, a maximum build height (up to 7 mm) was achieved under two distinct processing conditions: 1,000 W with a scanning speed of 35 mm/s, and 1,500 W with a scanning speed of 15 mm/s. Specifically, the former condition (1,000 W, 35 mm/s) resulted in minimal material mixing at the fusion boundary. All compositions exhibited a low density of defects, primarily in the form of unmelted powder particles located at the edges of the deposited structures. Cracking was most prevalent in the initial steel layers when employing higher laser power processing modes.

The chromium-to-nickel equivalent ratio correlated with the formation of mixing zones exhibiting distinct solidification modes and phase compositions. Specifically, deposition of *Inconel 625* onto *316L* steel resulted in a transition zone, characteristic of iron-based alloy compositions, exhibiting successive solidification modes: *FA* (ferrite–austenite), *AF* (austenite–ferrite), and *A* (austenite). Conversely, deposition of *316L* steel onto *Inconel 625* yielded a transition zone with exclusively austenite solidification. These phase identification results were confirmed by X-ray diffraction analysis. Scanning electron microscopy further confirmed the presence of ferrite in the interdendritic regions on the steel side.

Microhardness testing revealed minimal impact of deposition parameters on the average hardness of the materials. The microhardness of *316L* steel was consistently measured at 230 ± 15 HV, while that of *Inconel 625* averaged 298 ± 20 HV.

References

1. Zhang Y., Hu M., Cai Z., Han C., Li X., Huo X., Fan M., Rui S., Li K., Pan J. Effect of nickel-based filler metal types on creep properties of dissimilar metal welds between Inconel 617B and 10 % Cr martensitic steel. *Journal of Materials Research and Technology*, 2021, vol. 14, pp. 2289–2301. DOI: 10.1016/j.jmrt.2021.07.131.

2. Meng W., Zhang W., Zhang W., Yin X., Cui B. Fabrication of steel-Inconel functionally graded materials by laser melting deposition integrating with laser synchronous preheating. *Optics & Laser Technology*, 2020, vol. 131, p. 106451. DOI: 10.1016/j.optlastec.2020.106451.

3. Naffakh H., Shamanian M., Ashrafizadeh F. Dissimilar welding of AISI 310 austenitic stainless steel to nickel-based alloy Inconel 657. *Journal of Materials Processing Technology*, 2009, vol. 209 (7), pp. 3628–3639. DOI: 10.1016/j.jmatprotec.2008.08.019.

4. Reed R.C. *The superalloys: fundamentals and applications*. Cambridge, Cambridge university press, 2008. 363 p. ISBN 9780511541285. DOI: 10.1017/CBO9780511541285.

5. Knorovsky G.A., Cieslak M.J., Headley T.J., Romig A.D., Hammetter W.F. Inconel 718: A solidification diagram. *Metallurgical Transactions A*, 1989, vol. 20 (10), pp. 2149–2158. DOI: 10.1007/BF02650300.

6. Xie H., Yang K., Li F., Sun C., Yu Z. Investigation on the Laves phase formation during laser cladding of IN718 alloy by CA-FE. *Journal of Manufacturing Processes*, 2020, vol. 52, pp. 132–144. DOI: 10.1016/j.jmapro.2020.01.050.

7. Yang J., Zheng Q., Zhang H., Sun X., Guan H., Hu Z. Effects of heat treatments on the microstructure of IN792 alloy. *Materials Science and Engineering: A*, 2010, vol. 527 (4–5), pp. 1016–1021. DOI: 10.1016/j.msea.2009.10.026.

8. Rashkovets M.V. *Struktura i svoistva nikelevykh splavov, poluchennykh po additivnoi tekhnologii s ispol'zovaniem metoda pryamogo lazernogo vyrashchivaniya*. Diss. kand. tekhn. nauk [Structure and properties of nickel alloys obtained by additive technology using the direct laser deposition method. PhD, eng. sc. diss.]. Novosibirsk, 2022. 164 p.

9. Deshpande A. Additive manufacturing of nickel alloys. *Springer handbook of additive manufacturing*. Cham, Springer, 2023, pp. 655–669. ISBN 978-3-031-20751-8. DOI: 10.1007/978-3-031-20752-5_39.

10. Ahsan Md. R.U., Fan X., Seo G.-J., Ji C., Noakes M., Nycz A., Liaw P.K., Kim D.B. Microstructures and mechanical behavior of the bimetallic additively-manufactured structure (BAMS) of austenitic stainless steel and Inconel 625. *Journal of Materials Science & Technology*, 2021, vol. 74, pp. 176–188. DOI: 10.1016/j.jmst.2020.10.001.

11. Carroll B.E., Otis R.A., Borgonia J.P., Suh J., Dillon R.P., Shapiro A.A., Hofmann D.C., Liu Z.-K., Beese A.M. Functionally graded material of 304L stainless steel and Inconel 625 fabricated by directed energy deposition: Characterization and thermodynamic modeling. *Acta Materialia*, 2016, vol. 108, pp. 46–54. DOI: 10.1016/j.actamat.2016.02.019.

12. Li P., Gong Y., Xu Y., Qi Y., Sun Y., Zhang H. Inconel-steel functionally bimetal materials by hybrid directed energy deposition and thermal milling: Microstructure and mechanical properties. *Archives of Civil and Mechanical Engineering*, 2019, vol. 19 (3), pp. 820–831. DOI: 10.1016/j.acme.2019.03.002.

13. Tyagi S., Balla S.K., Manjaiah M., Aranas C. Microstructure and mechanical properties of stainless steel 316L-Inconel 625 bimetallic structure fabricated by laser wire direct energy deposition. *Journal of Materials Research and Technology*, 2024, vol. 33, pp. 8361–8371. DOI: 10.1016/j.jmrt.2024.11.130.

14. Ghanavati R., Naffakh-Moosavy H., Moradi M., Mazzucato F., Valente A., Bagherifard S., Saboori A. Design optimization for defect-free AISI 316 L/IN718 functionally graded materials produced by laser additive manufacturing. *Materials Characterization*, 2025, vol. 220, p. 114697. DOI: 10.1016/j.matchar.2024.114697.

15. Li Y., Koukolíková M., Džugan J., Brázda M. High temperature fracture behavior of 316L stainless steel-Inconel 718 functionally graded materials manufactured by directed energy deposition: Role of interface orientation and heat treatment. *Materials Science and Engineering: A*, 2024, vol. 898, p. 146389. DOI: 10.1016/j.msea.2024.146389.

16. Dolgova S.V., Malikov A.G., Golyshev A.A., Nikulina A.A. The effect of laser surfacing modes on the geometrical characteristics of the single laser tracks. *Obrabotka metallov (tekhnologiya, oborudovanie, instrumenty) = Metal Working and Material Science*, 2024, vol. 26, no. 2, pp. 57–70. DOI: 10.17212/1994-6309-2024-26.2-57-70.

17. Chen N., Khan H.A., Wan Z., Lippert J., Sun H., Shang S.-L., Liu Z.-K., Li J. Microstructural characteristics and crack formation in additively manufactured bimetal material of 316L stainless steel and Inconel 625. *Additive Manufacturing*, 2020, vol. 32, p. 101037. DOI: 10.1016/j.addma.2020.101037.

18. Everton S.K., Hirsch M., Stravroulakis P., Leach R.K., Clare A.T. Review of in-situ process monitoring and in-situ metrology for metal additive manufacturing. *Materials & Design*, 2016, vol. 95, pp. 431–445. DOI: 10.1016/j.matdes.2016.01.099.

19. Mei X., Wang X., Peng Y., Gu H., Zhong G., Yang S. Interfacial characterization and mechanical properties of 316L stainless steel/Inconel 718 manufactured by selective laser melting. *Material Science and Engineering: A*, 2019, vol. 758, pp. 185–191. DOI: 10.1016/j.msea.2019.05.011.

20. Villaret F., Boulnat X., Aubry P., Yano Y., Ohtsuka S., Fabrègue D., De Carlan Y. Laser Beam Direct Energy Deposition of graded austenitic-to-martensitic steel junctions compared to dissimilar Electron Beam welding. *Materials Science and Engineering: A*, 2021, vol. 824, p. 141794. DOI: 10.1016/j.msea.2021.141794.

21. Astafurov S., Astafurova E. Phase composition of austenitic stainless steels in additive manufacturing: A review. *Metals*, 2021, vol. 11 (7), p. 1052. DOI: 10.3390/met11071052.

22. Pouranvari M., Khorramifar M., Marashi S.P.H. Ferritic–austenitic stainless steels dissimilar resistance spot welds: metallurgical and failure characteristics. *Science and Technology of Welding and Joining*, 2016, vol. 21 (6), pp. 438–445. DOI: 10.1080/13621718.2015.1124491.

Conflicts of Interest

The authors declare no conflict of interest.